Steel and Composite Structures, *Vol. 36, No. 5 (2020) 533-551*
DOI: https://doi.org/10.12989/scs.2020.36.5.533

Seismic performance of the concrete-encased CFST column to RC beam joints: Analytical study

Dan-Yang Ma[1a], Lin-Hai Han[*1], Xiao-Ling Zhao[2b] and Wei-Biao Yang[3c]

[1]*Department of Civil Engineering, Tsinghua University, Beijing, 100084, P.R. China*
[2]*Department of Civil and Environmental Engineering, The University of New South Wales (UNSW), Sydney, NSW 2052, Australia*
[3]*Beijing Institute of Architectural Design, Beijing 100045, P.R. China*

(*Received October 3, 2019, Revised July 8, 2020, Accepted August 8, 2020*)

Abstract. A finite element analysis (FEA) model is established to investigate the concrete-encased concrete-filled steel tubular (CFST) column to reinforced concrete (RC) beam joints under cyclic loading. The feasibility of the FEA model is verified by a set of test results, consisting of the failure modes, the exposed view of connections, the crack distributions and development, and the hysteretic relationships. The full-range analysis is conducted to investigate the stress and strain development process in the composite joint by using this FEA model. The internal force distributions of different components, as well as the deformation distributions, are analyzed under different failure modes. The proposed connections are investigated under dimensional and material parameters, and the proper constructional details of the connections are recommended. Parameters of the beam-column joints, including material strength, confinement factor, reinforcement ratio, diameter of steel tube to sectional width ratio, beam to column linear bending stiffness ratio and beam shear span ratio are evaluated. Furthermore, the key parameters affecting the failure modes and the corresponding parameters ranges are proposed in this paper.

Keywords: joint; seismic performance; concrete-encased CFST column; reinforced concrete(RC) beam; finite element analysis (FEA); full-range analysis

1. Introduction

Concrete-encased concrete-filled steel tubular (CFST) column can be conveniently connected to RC beams to form beam-column joints (Han *et al*. 2018). Fig. 1 shows the application of various beam-column joints in a frame structure, including the interior joint I, the double beam joint II, the exterior joint III, the staggered joint IV and the unsymmetrical joint V. Though these composite joints have many applications, there is a lack of numerical modelling of the seismic performance and its failure mechanism.

The seismic performance of conventional RC joints has been continuously studied since the 1970s, and the RC joints have been numerically studied by many researchers (Lee *et al*. 2009). Moustafa and Mosalam (2015) studied the seismic response of RC pier to bent cap joints. It was found that the slab width and slab reinforcement should be included for capacity estimation, especially in tension. A numerical model for RC beam-column joints was proposed by Lima *et al*. (2017) based on the pivot model. The model could reasonably predict the cyclic behaviour of conventional RC joints and could be used in the frame structures. De Risi and Verderame (2017) simulated the RC beam-column joints with fibre model, while the seismic response was not analyzed. Li and Leong (2015) analyzed the cyclic behaviour of RC beam-column joints under a three-dimensional model, which got reasonably verification with test results. Since the stress state of longitudinal rebars could be applied to justify the bond-slip relationship between concrete and longitudinal rebars (Moustafa and Mosalam 2015). It was found that the axial load could increase the bond stress of longitudinal rebars in the panel zone. A rigid-plastic model was proposed by Kang and Tan (2017) to investigate the RC beam-column joints. The rebar slippage and rotation of the panel zone were considered in the model, and the maximum strength of the joint could be calculated based on the force equilibrium at the joint interface. However, the hysteretic curve could not be obtained based on this model. Hwang *et al*. (2017) put forward the shear strength degradation model for the RC beam-column joints. The failure mode was classified by the bar-bond failure and the panel zone shear failure, while the bar-bond strength could be guaranteed by effective connections in the composite joints. Due to the limited research method, the conventional RC beam-column joints were mostly analyzed by the simplified model. The studied axial load level was mostly below 0.5, which indicated the conventional RC beam-column joints were not applicable to sustain high axial load, especially under cyclic load.

*Corresponding author, Professor
E-mail: lhhan@tsinghua.edu.cn
[a]Ph.D.
E-mail: mady@tsinghua.edu.cn
[b]Professor
E-mail: xiaolin.zhao@unsw.edu.au
[c]Senior Engineer
E-mail: yang-weibiao@vip.sina.com

http://www.techno-press.org/?journal=scs&subpage=8
ISSN: 1229-9367 (Print), 1598-6233 (Online)

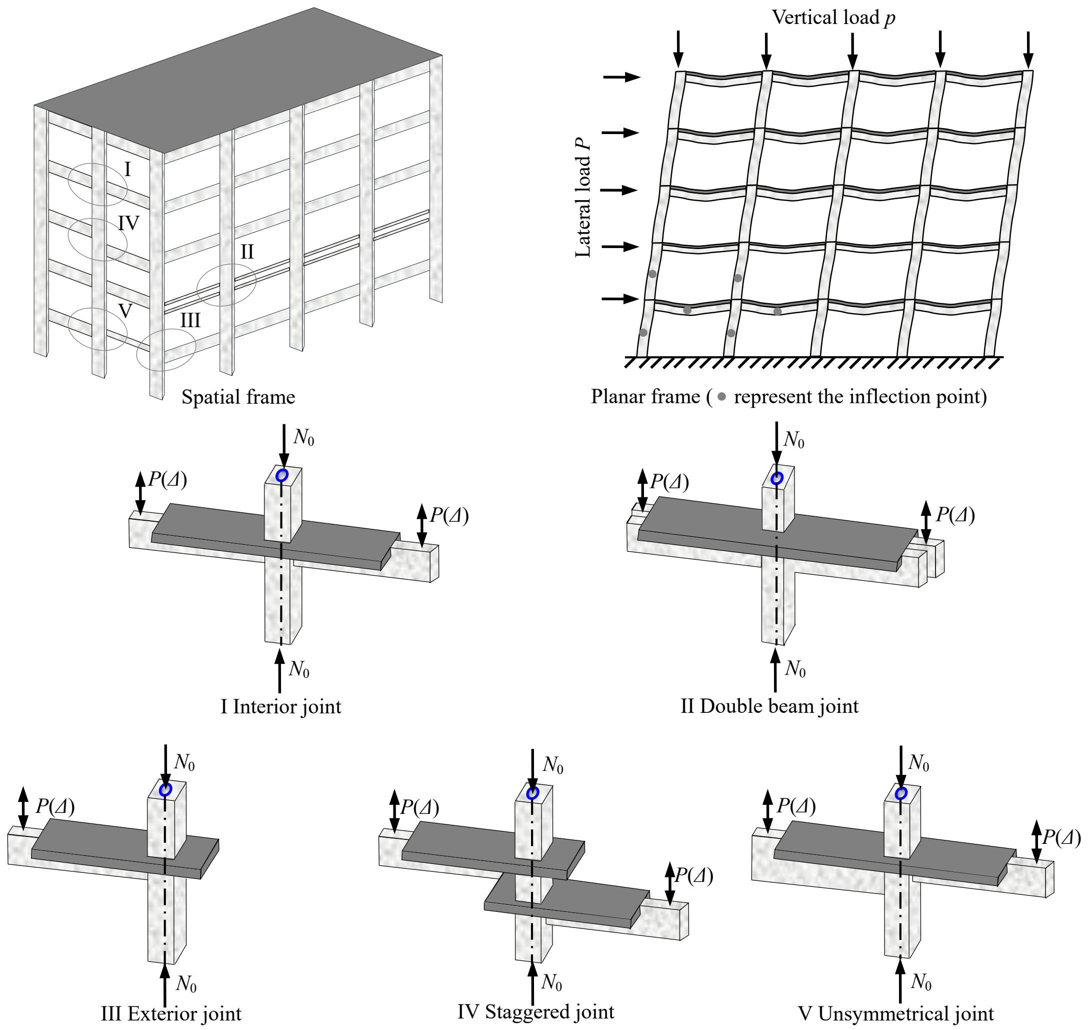

Fig. 1 Applications of concrete-encased CFST column to RC beam joint

The joints with CFST columns behaved similarly to the joints with concrete-encased CFST columns. The seismic performance of joints with CFST columns was widely analyzed by former researchers. Li *et al*. (2011) conducted a FE analysis for the beam-column joints composed of CFST column and steel beam. A parameter study was carried out on the failure modes, maximum strength and ductility, and various failure modes were identified by the beam to column bending capacity ratio. The CFST column to steel beam joints were also subjected to cyclic loading with bolt connection (Lai *et al*. 2017, De Nardin and El Debs 2018). The load-displacement relationships of bolt connections were firstly simulated by solid element and then were applied in the fibre model of composite joints. The fibre model was then used to evaluate load-displacement relationships of these joints. Chen *et al*. (2014) investigated the CFST column to RC beam joints analytically. The reinforcement ratio and the axial compressive force were evaluated through the parametric studies. While the model could only simulate the monotonic loading behaviour of the composite joint, the cyclic behaviour was not studied by FEA model. The joints with CFST columns were mostly analyzed by the three- dimensional model. The studied axial load level was under 0.6, which was higher than the conventional RC joints, which indicated the ductile behaviour of the joints with CFST columns. The shear strength of CFST column joints were analysed and applied in the fibre model, which showed good agreement with the test results (Kang *et al*. 2015).

From the aforementioned research, it was found that the joints with CFST columns could sustain high axial load level under cyclic loading with favorable ductility. The composite joints with concrete-encased CFST columns could reduce the steel tube dimension compared to the joint with CFST columns, and the outer concrete could protect the steel tube from local buckling, which was beneficial for the seismic performance. In spite of the general lack of analysis on the seismic performance of the concrete-encased CFST column to RC beam joints, the simulation of that kind of joint has been conducted by Zhang *et al*. (2018). A tri-linear restoring force model was proposed based on the FEA model, nevertheless, the simulated hysteretic curve could not reflect the pinching phenomenon for the concrete cracking behaviour was not considered in the model. This paper aims to present a numerical analysis

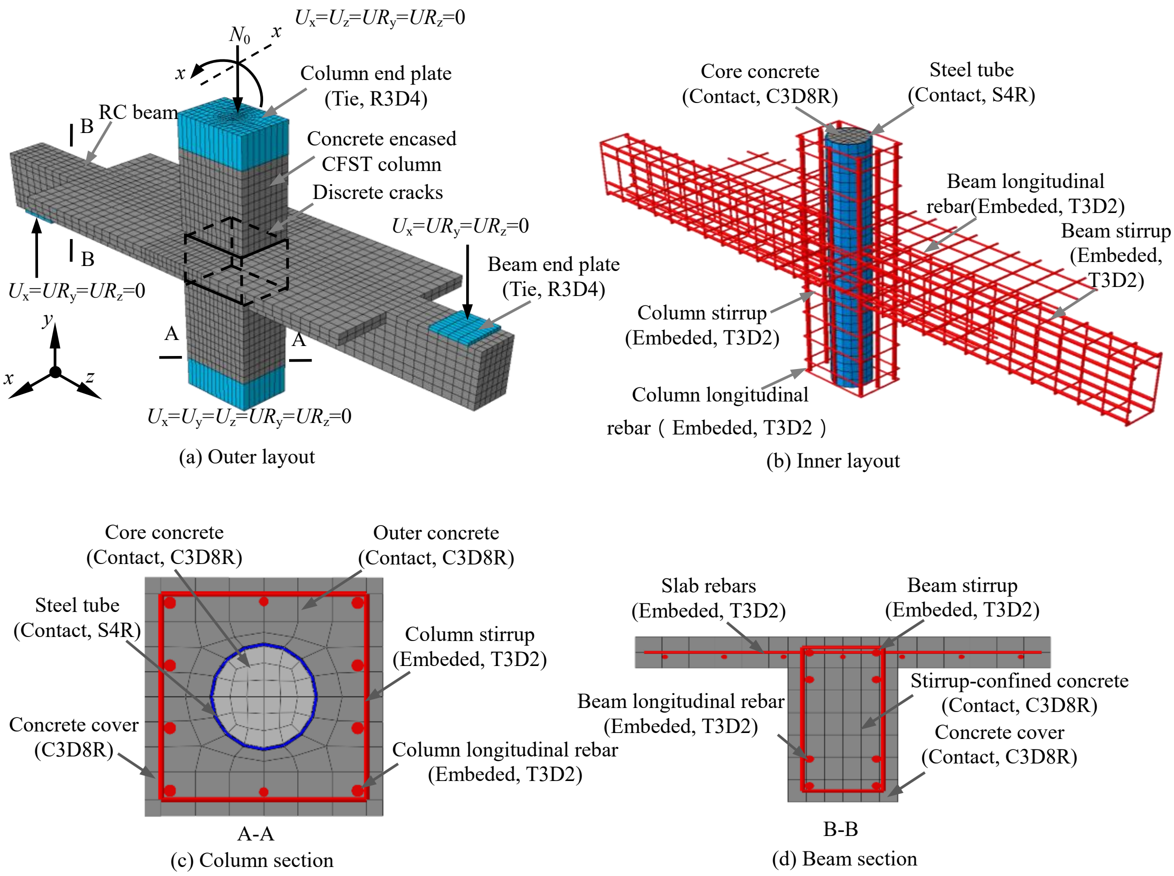

Fig. 2 Schematic view of FEA model

of the seismic performance of the composite joints, which could provide the internal force distributions and the deformation distributions of the composite joints. Furthermore, the constructional details of the connections could be investigated based on the FEA model. Besides, the verified FEA model made it possible to conduct a large amount of parameter analysis to define the parameter ranges of typical failure modes.

2. FEA modelling

The beam-column joint model was established to analyze the joints introduced in the companion paper (Ma *et al*. 2019) based on the ABAQUS/Standard module (Simulia 2017). Fig. 2 illustrated the schematic view of the beam-column joint FEA model. The details of other joints (i.e., joint types I, II, III, IV and V) could be found in Fig. 1 and the companion paper (Ma *et al*. 2019).

2.1 materials

The material properties of concrete and steel were both considered by monotonic behaviour and hysteretic behaviour separately. For concrete, the concrete damaged plasticity (CDP) model (Lee and Fenves 1998) could consider the degradation of concrete and be used to simulate the hysteretic behaviour of concrete. The strength improvement of concrete under 3-D stress state could be achieved by considering the lateral confining pressure of concrete in the three-dimensional model, while the ductility improvement was not considered sufficiently. Therefore, the column section and the beam section were divided into three and two regions respectively, as shown in Figs. 2(c) and 2(d). The section division could define the stress-strain relationships of core concrete (Han *et al*. 2007), outer stirrup-confined concrete (Han and An 2014) and concrete cover (Attard and Setunge 1996) respectively. In that circumstance, the confinements and ductility improvement could be taken into consideration. The uniaxial strength of three kinds of concrete was the same as shown in Fig. 3(a). In order to consider the degradation of concrete under cyclic loading, Li and Han (2011) proposed the assumption of “focal points”. The hysteretic behaviour of core concrete was shown in Fig. 3(b) as an example. The compressive damage variable d_c and tensile damage variable d_t have been defined in the “focal points” assumption (Li and Han 2011). The recovery stiffness factors ω_c and ω_t defined the stiffness recovery as the load changes from tension to compression and on the contrary, respectively. The compressive stiffness recovery factor ω_c was set as 0.5 for the outer concrete. Meanwhile, the compressive stiffness recovery factor ω_c was set as 1 for core concrete to consider the confinements (Ma *et al*. 2017). The tensile recovery stiffness factor ω_t was set as 0 for all concrete.

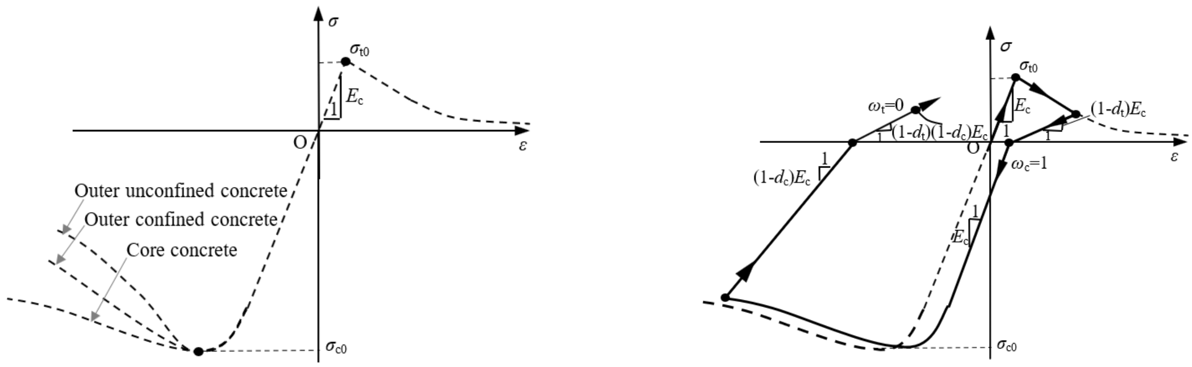

(a) Monotonic behaviour of three kinds of concrete (b) Hysteretic behaviour of core concrete

Fig. 3 Stress-strain relationships of concrete

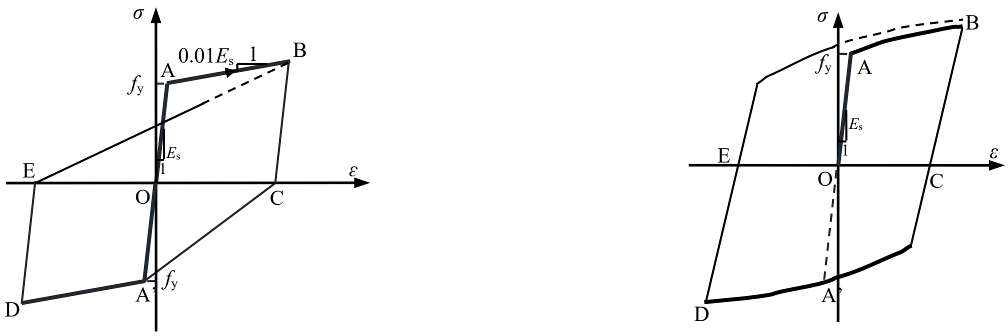

(a) Hysteretic behaviour of steel rebars (b) Hysteretic behaviour of steel tube

Fig. 4 Stress-strain relationships of steel

As the tensile behaviour was slightly influenced by the confinements, the unified uniaxial tensile model (Shen *et al.* 1993) was drawn on three types of concrete. The concrete elastic modulus E_c was set as $4730\sqrt{f_c^{'}}$ (MPa), according to ACI318-14 (2014). Moreover, the concrete Poisson's ratio was set as 0.2.

For the monotonic behaviour of steel components, the steel components followed the Von-Mises yield criterion. Considering the strain-hardening effects, the hardening modulus of $0.01E_s$ was applied in the isotropic hardening rule as shown in Fig. 4(a). For the hysteretic behaviour of steel components, the Bauschinger effects were considered in both steel tube and rebars. The Clough model (Clough 1966) was used to simulate the longitudinal rebars for the reason that the Clough model could consider the slippage effects to some extent, which could not be directly considered in the interaction behaviour. Although the Clough model could not consider the slippage meticulously, it was the most efficient method currently. The combined hardening model was used to simulate the steel tube, the model of which could consider the Bauschinger effects and isotropic behaviour under cyclic loading simultaneously as shown in Fig. 4(b). The parameters defining the cyclic behaviour were determined according to the previous study of CFST members (Han and Yang 2005).

2.2 Interaction

The steel tube and its surrounding concrete were connected by the surface contact interaction, the parameter of which could refer to past researchers (Ma *et al.* 2017, Ma *et al.* 2018, Qian *et al.* 2016).

Though the concrete damaged plasticity model could consider the damage and degradation of concrete, the opening and closure of cracks (Goto *et al.* 2010) were not considered in the constitute model. Four discrete cracks were set up to take this effect into consideration. Since the cracks focused on the region between panel zone and members in the test, these discrete cracks lied in the boundary of the panel zone and beam ends, as well as the boundary of the panel zone and column ends as shown in Fig. 2. For the sake of simulating the cracks, the "hard" contact and Coulomb friction were applied in the normal direction and tangential direction separately. The frictional parameters could refer to the provision of ACI 318-14 (2014). Through applying the discrete cracks in the model, the opening and closure of cracks could be simulated in the model. Moreover, the reasonable pinching phenomenon in the hysteretic curve could be captured to a certain extent.

The column end plate and beam end plate were connected strongly with the column and beam respectively in the test. Therefore, the "tie" constraint was used to connect the column end plate and column, and the same constraint was used between beam end plate and the beam.

The longitudinal rebars were connected to the connections by "coupling" within the welding length, and the rest parts of rebars were "embedded" in the outer concrete. The nodes of rebar within the welding length and anchorage range were coupled to the corresponding nodes in the connections. The aforementioned interactions were illustrated in Fig. 2.

2.3 Boundary condition and mesh

The loading boundary condition was the same as that in the test (Ma *et al*. 2019) and also shown in Fig. 5. The axial load was applied on the column end plate, which was tied to the top surface of the column. The upper column end plate was constrained in the displacements along the x and z axes and rotations in the xz and xy planes. The bottom column end plate was additionally constrained in the displacement along y axis. The cyclic loading was applied on the beam end plate, which was tied to the surface of the beam. The beam end plate was constrained in the displacements along the x axis and rotations in the xz and xy planes. The loading procedure could refer to the test loading procedure. The constant axial load was applied on the upper column end plate in advance. Afterwards, the cyclic vertical load was imposed on the beam end plates.

8-node three-dimensional solid elements were used to simulate the concrete. 4-node shell elements were used to simulate the steel tubes and connections. 4-node shell rigid elements were used to simulate the end plates. Both the solid elements and shell elements were simulated in reduced integration. 2-node linear truss elements were used to simulate the longitudinal rebars and stirrups. The sensitivity analysis was conducted and the typical mesh sensitivity could be seen in Figs. 2(a) and 2(b).

3. Validations of the FEA model

The connections and joint types in the previous research (Liao *et al*. 2014, Xiang *et al*. 2017) were different from those in this paper. Furthermore, the failure modes in the previous research were mainly beam bending failure, which has been studied in this paper. Therefore, the established beam-column joints model, as introduced above, was only verified by the test results in the companion paper (Ma *et al*. 2019). The measured and calculated results were shown in Table 1. Although the conservative predictions were obtained in some specimens (J3-1, J5-1 & J5-2), which was due to the uniform strength degradation parameters of concrete. The mean value of the predicted maximum strength to measured maximum strength ratio P_{uc}/P_{ue} was 0.955 and the corresponding standard deviation was 0.068. It could be concluded that the FEA model could make an appropriate simulation of the joint bearing capacity.

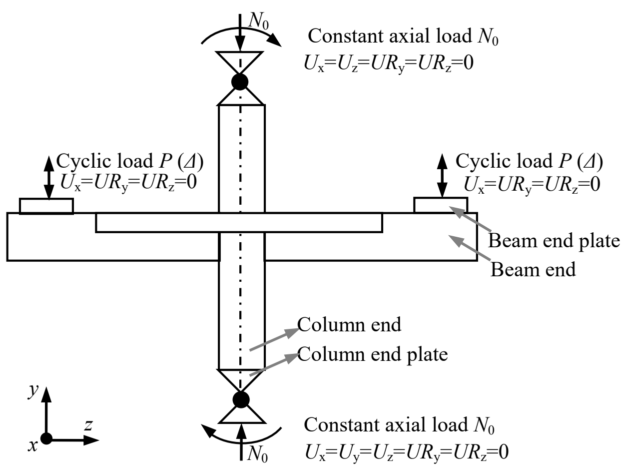

Fig. 5 Boundary conditions of joints

3.1 Brief summary of experimental results

The seismic performance of that kind of composite joints has been experimentally investigated (Ma *et al*. 2019). Thirteen plane beam-column joints in transverse and longitudinal directions were studied separately, which could represent the spatial joint in the actual engineering. The constant axial load was applied to the column in advance. The cyclic vertical load was imposed on the beam afterwards. The failure modes of the beam-column joints could be classified to four types. Failure mode A is beam bending failure and failure mode B is beam bending-shear failure. Failure mode C and failure D are column compression-bending failure and panel zone shear failure, respectively. Each failure mode was determined by the bearing capacity of the corresponding component. Though the load versus displacement relationships have already been studied in the experimental study, the stress state of concrete and steel components could not be captured. Although diverse connections have been proposed for the concrete-encased CFST column to RC beam joints in previous research, including holes in steel tube, ring beam, steel bracket. Four types of connections were proposed to connect the longitudinal rebars in beam to the steel tube in the column effectively in this study, e.g., ring plate connection, sleeve connection, wing plate connection, and anchorage connection. It was found that the connections kept intact in the test. For the conventional RC joints, the failure modes could be classified as shear failure and bond failure (Lee *et al*. 2009). Actually, the bond failure could be avoided by the connections in the beam-column joints discussed in this paper. More details about the experimental results can be found in the companion paper (Ma *et al*. 2019).

3.2 Failure modes

The verifications of typical failure modes for the joint specimens were shown in Fig. 6. For different failure modes, concrete crack distributions could reflect the characteristic of the failure mode, which was represented by the equivalent plastic strain (PEEQ) in the FEA model. The PEEQ distributions in the predicted failure modes were consistent with the observed failure modes, and the simulated plastic hinge length and the main diagonal crack coincided approximately with the observed failure modes. It

Table 1 Summary of measured and predicted results

Specimen	Failure modes	Axial load level n	Measured maximum strength P_{ue} (kN) +	Measured maximum strength P_{ue} (kN) -	Predicted maximum strength P_{uc} (kN) +	Predicted maximum strength P_{uc} (kN) -	Predicted beam strength P_b (kN)	Predicted column strength P_c (kN)	Predicted panel zone strength P_j (kN)	Average maximum strength ratio P_{uc}/P_{ue}
J1-1	Panel zone shear failure	0.6	107	-109	107	-92	111	135	92/209	0.922
J1-2	Beam bending failure	0.6	106	-144	107	-131	111	269	183/418	0.960
J2-1	Column compression-bending failure	0.6	569	-533	503	-501	589	509	538/1341	0.912
J3-1	Panel zone shear failure	0.6	185	-170	144	-165	162	207	144/245	0.874
J4-1	Column compression-bending failure	0.2	432	-440	438	-458	485	417	318/661	1.027
J4-2	Beam bending-shear failure	0.2	200	-207	182	-208	188	359	190/325	0.957
J4-3	Beam bending-shear failure	0.47	193	-194	180	-200	188	266	192/350	0.982
J4-4	Beam bending-shear failure	0.2	198	-202	187	-192	188	359	219/363	0.947
J4-5	Beam bending-shear failure	0.2	261	-266	287	-269	233	375	261/298	1.055
J4-6	Beam bending failure	0.2	67	-64	63	-72	65	331	141/127	1.033
J5-1	Beam bending failure	0.2	92	-95	70	-85	83	278	112/124	0.828
J5-2	Beam bending failure	0.6	86	-88	72	-84	83	192	119/138	0.896
J6-1	Beam bending failure	0.2	61	-78	62	-79	61	331	141/211	1.015
Mean										0.955
COV										0.068

indicates that the FEA model could predict the spalling and crushing of concrete. Although the diagonal cracks in the beam bending-shear specimen J4-2 were not reflected by the PEEQ distributions directly, the predicted main diagonal cracks region was consistent with the measured results. The exposed view of the inner steel components was also shown in Fig.6. The Von Mises stress could justify the stress state of steel components, therefore the Von Mises stress distributions were compared with the observed exposed view of the inner steel components. The yielding state of steel tube and rebars were consistent with the corresponding steel component in the test. It indicated that the stress state of inner steel components was well predicted.

The connections remained intact during the whole loading procedure in the test. In the FE analysis, the Von Mises stresses of the corresponding connections were still lower than the yield stress as shown in Fig. 7. Besides, the FEA model could capture the failure mode of concrete components and inner steel components.

3.3 Crack distributions

The panel zone shear failure joint J1-1 was selected to verify the crack distributions and development as shown in Fig. 8. Since the cracks in the slab were measured in the vertical view during the test, the experimental crack distributions at $2\Delta_y$ were shown in both the front view and vertical view in Fig. 8(a). The loading degree $2\Delta_y$ also indicated the maximum strength of the joint J1-1. The layout of the cracks was depicted in red lines. Meanwhile, the crack width was illustrated beside the measured crack and was shown in brackets.

The crack distribution was represented by the tensile damage in the analysis and the tensile damage distribution at $0.25P_y$ was shown in Fig. 8(b). Since the left beam was firstly subjected to the upward loads, the bottom region of the left beam had more severe damage than the right beam, which was in coincidence with the experimental results. The tensile damage distribution at Δy was shown in Fig. 8(c). The left beam and right beam obtained similar tensile damage in the analytical results, which matched well with the experimental observation. The cracks distributed symmetrically between the left beam and the right beam at Δ_y. Therefore, the FEA model could capture the crack distributions at the yield loading. The joint J1-1 reached the ultimate strength at $2\Delta_y$ and the corresponding tensile damage distribution was shown in Fig. 8(d). The damage in the beam kept constant from Δ_y to $2\Delta_y$, while the damage in the panel zone differed much in this loading procedure. Meanwhile, the crack width in the panel zone increased from 0.05 mm to 0.2 mm with the loading degree increasing from $0.25P_y$ to $2\Delta_y$. The further development of crack width was not measured due to the concrete spalling after $2\Delta_y$. In summary, the FEA model could capture the crack distributions and development by considering the tensile damage in the joints.

3.4 Hysteretic relations

Comparisons between the measured and predicted hysteretic relationships were shown in Fig. 9. The predicted failure mode was consistent with the experimental failure mode, which was shown in Fig. 6.

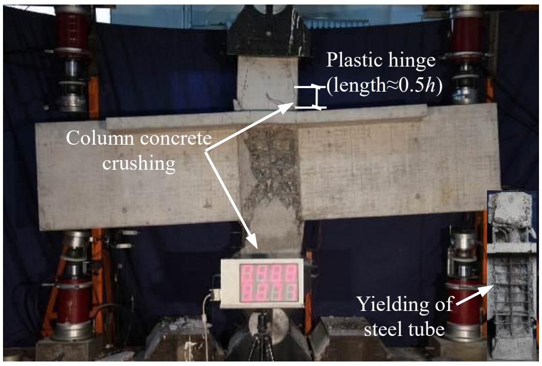

(a) J4-1 (Observed, Column compression-bending failure)

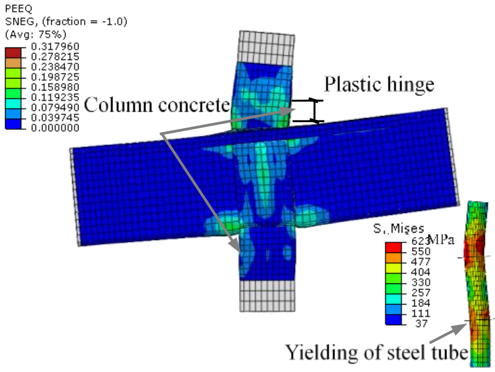

(b) J4-1 (Predicted, Column compression-bending failure)

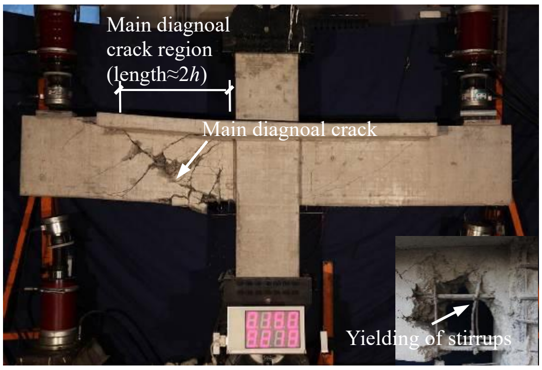

(c) J4-2 (Observed, Beam bending-shear failure)

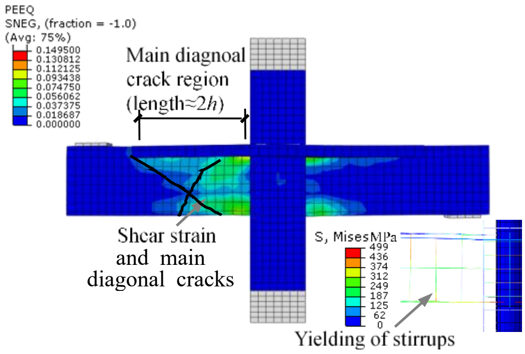

(d) J4-2 (Predicted, Beam bending-shear failure)

(e) J1-2 (Observed, Beam bending failure)

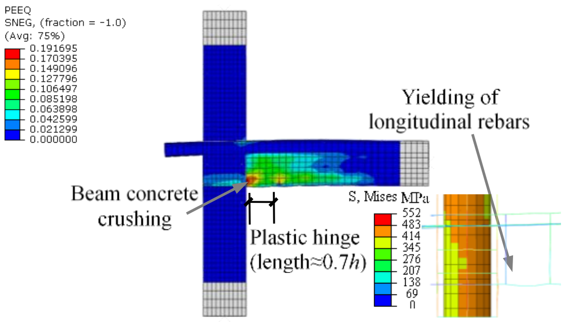

(f) J1-2 (Predicted, Beam bending failure)

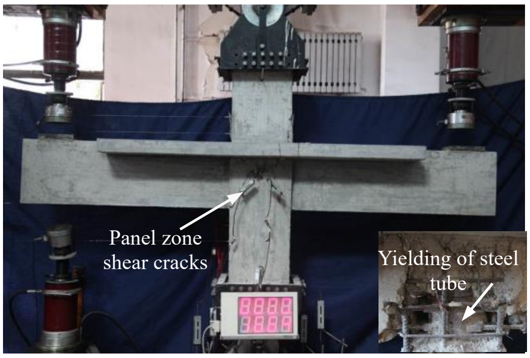

(g) J3-1 (Observed, Panel zone shear failure)

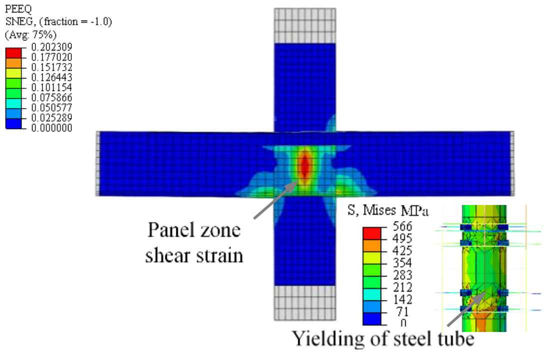

(h) J3-1 (Predicted, Panel zone shear failure)

Fig. 6 Verification of failure modes

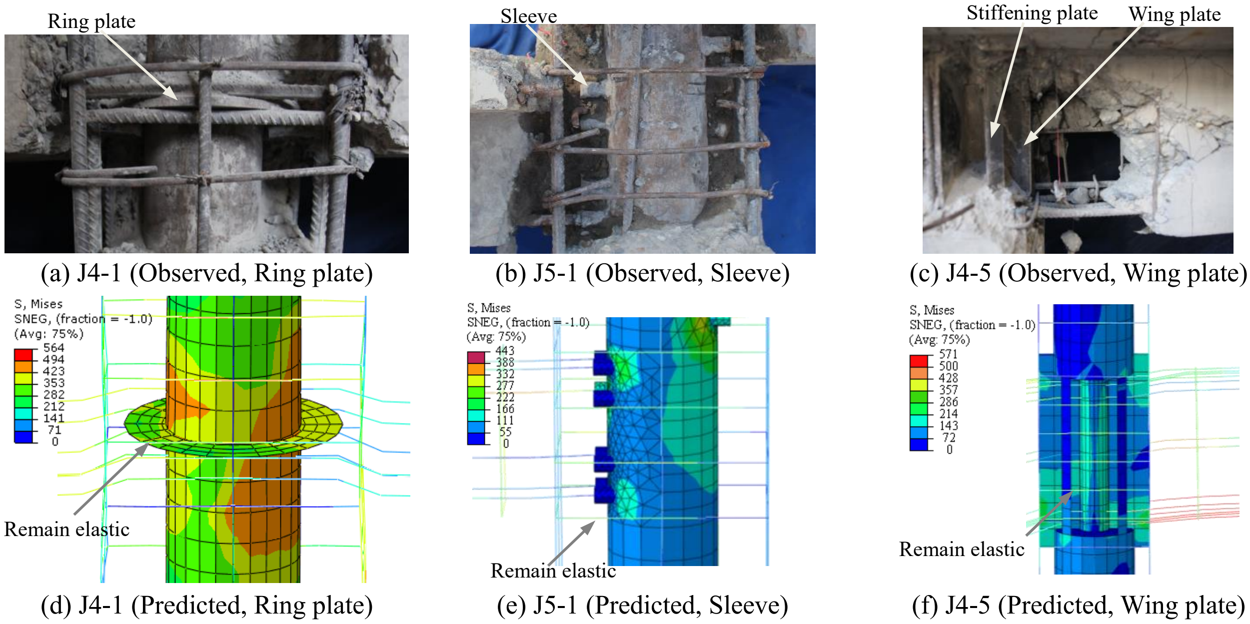

Fig. 7 Verification of exposed view of connections (Unit: MPa)

Therefore, the predicted strength could represent the strength of the corresponding components, including beam, column and panel zone. With the consideration of the material degradation and the cracking of concrete, the loading and unloading stiffness were predicted approximately comparing to the measured one. Moreover, the pinching phenomenon was also captured in most of specimens. While the predicted descending branch was smoother than the measured one, e.g. J4-1, J6-1, for the spalling and crushing of concrete were not fully considered in the FEA model. The predicted curve of some specimens, e.g., J4-1, J4-3, and J4-5, were plumper than the measured curve, which could attribute to two aspects. For the column compression-bending failure joint J4-1, the opening and closure of cracks were not be fully captured, especially under a high axial load level. For the beam bending-shear failure joints J4-3 and J4-5, the slippage along diagonal cracks caused the pinching phenomenon, which could not be fully considered in the FEA model. In general, the FEA model reached a reasonable agreement with the measured results.

Furthermore, the strength of internal components in beam-column joints was also evaluated by the existing calculation method, as shown in Table 1. Firstly, the RC beam strength included the bending strength and the shear strength, both of which could be calculated by the design code ACI 318(2019). The lower value could represent the strength of RC beam and be used to compare with the test results. Secondly, the strength calculation method of the composite column has been proposed by An and Han (2014), and the method was used to calculate the compression bending strength of the composite column. Finally, the shear strength of panel zone was also calculated based on the related research (Qian 2017) and design code CECS188(2019). To compare the calculation results and the test results, P_b, P_c and P_j are the vertical loads applied on the beam end corresponding to the strength of beam, compression bending strength of column and shear strength of joint, which were illustrated in Table 1. The first value of P_j is calculated by Qian (2017), and the second value was calculated by CECS188(2019).

It seems that the existing calculation method could reasonably predict the bending strength of beam and the compression-bending strength of column. However, there is much difference between the calculated shear strength of panel zone and the measured strength, especially for the column compression-bending failure joint (J4-1) and beam bending shear failure joints (J4-2 and J4-3). The panel zone failure would occur in the joint J4-1 according to the calculation method, whereas the column compression-bending failure actually occurred. It was due to the underestimate of panel zone shear strength in the current calculation method. Moreover, the shear strength calculated by two methods differed much from each other. Therefore, there is an urgent need to distinguish the failure modes. Based on the predicted failure mode, the existing calculation method could be applied to predict the strength under the beam and column failure mode. For the shear strength of panel zone, it requires more analytical study in further research.

4. Analytical results

4.1 Load versus displacement relationships

Four typical FEA joint models were established using the verified model corresponding to the test specimens, including the joint type II, joint type III, joint type IV and joint type V.

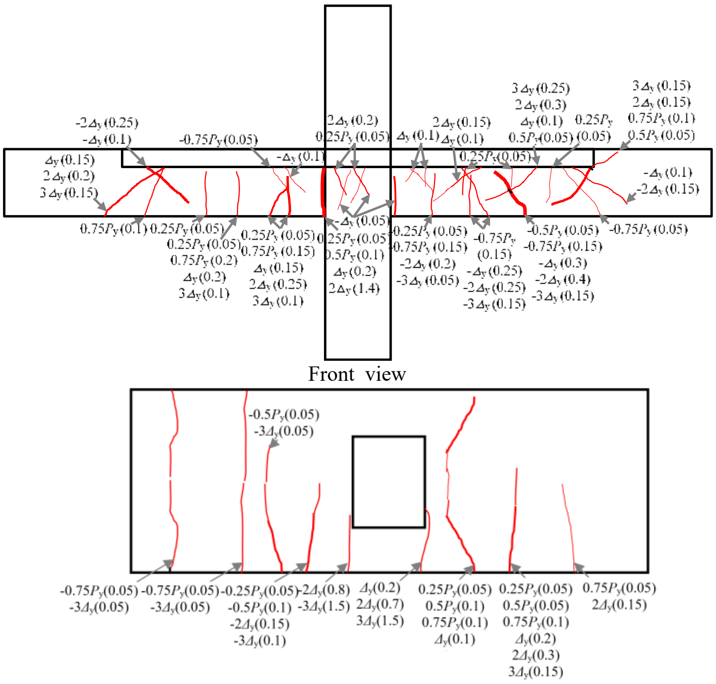

(a) Crack distritubiton of J1-1 at $2\Delta_y$ (Observed)

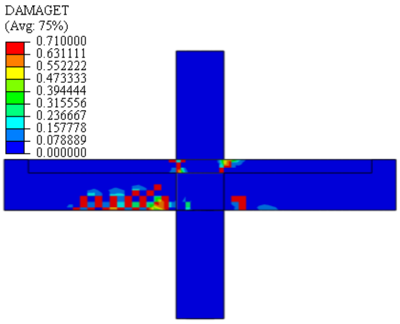

(b) Tensile damage distritubiton at $0.25P_y$ (Predicted)

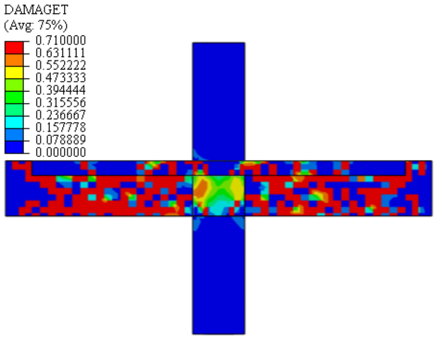

(c) Tensile damage distritubiton at Δ_y (Predicted)

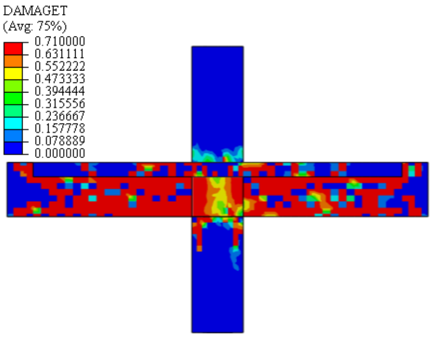

(d) Tensile damage distritubiton at $2\Delta_y$ (Predicted)

Fig. 8 Verification of crack distributions and development

The other two types of joints (joint type I with rectangular column and square column) described in the tests could refer to the aforementioned four typical joints. The dimensions of these joints were the same as the test joints J1-1, J2-1, J5-1 and J6-1. Conventional materials were used for these typical models, i.e. The yield strength of steel tube f_{ys} = 345 MPa; the yield strength of rebars $f_{yl} = f_{yh}$ = 335 MPa; the cube strength of outer concrete and core concrete $f_{cu,out}$ = 40 MPa, $f_{cu,core}$ = 60 MPa. The stress and strain development of these joints were analyzed based on the joint models, which could reflect the characteristics of four typical failure modes.

Fig. 10 shows the typical hysteretic relationships of beam-column joints under four typical failure modes, and Fig. 11 shows the typical principal tensile strain distribution when the maximum strength was reached. The joint J1-1

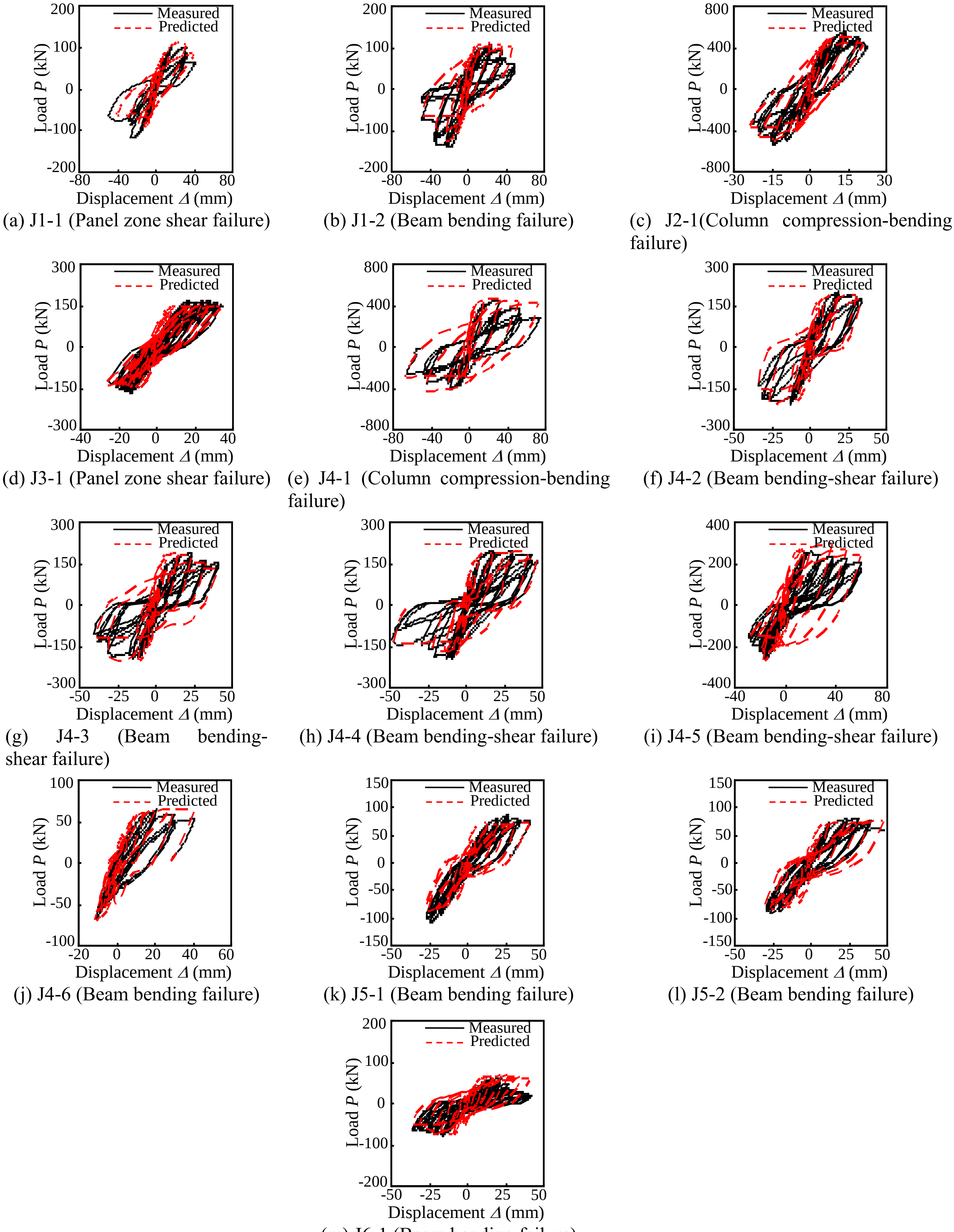

(a) J1-1 (Panel zone shear failure)
(b) J1-2 (Beam bending failure)
(c) J2-1(Column compression-bending failure)
(d) J3-1 (Panel zone shear failure)
(e) J4-1 (Column compression-bending failure)
(f) J4-2 (Beam bending-shear failure)
(g) J4-3 (Beam bending-shear failure)
(h) J4-4 (Beam bending-shear failure)
(i) J4-5 (Beam bending-shear failure)
(j) J4-6 (Beam bending failure)
(k) J5-1 (Beam bending failure)
(l) J5-2 (Beam bending failure)
(m) J6-1 (Beam bending failure)

Fig. 9 Verification of hysteretic relationships

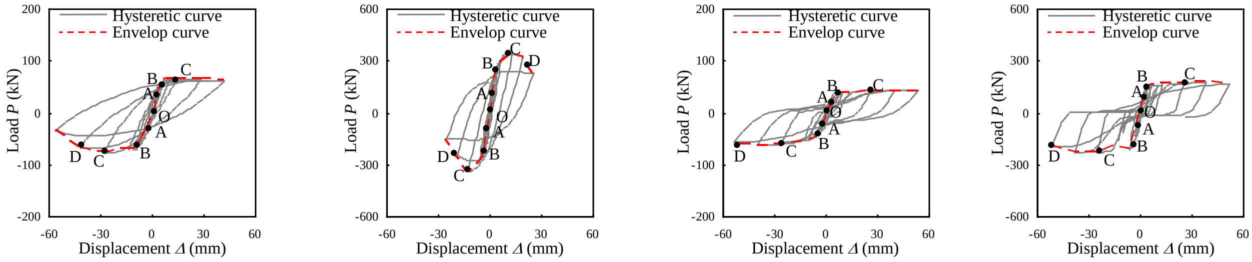

(a) J1-1 (Panel zone shear failure) (b) J2-1 (Column compression-bending failure) (c) J5-1 (Beam bending failure) (d) J6-1 (Beam bending-shear failure)

Fig. 10 Typical hysteretic relationships

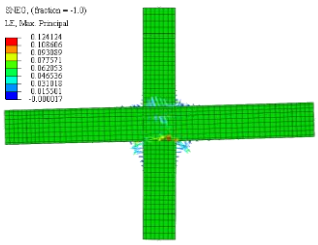

(a) J1-1 (Panel zone shear failure)

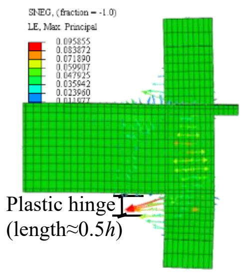

(b) J2-1 (Column compression-bending failure)

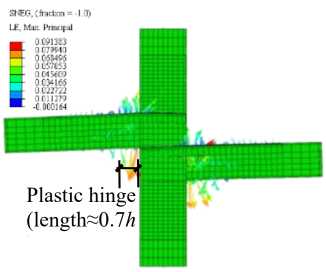

(c) J5-1 (Beam bending failure)

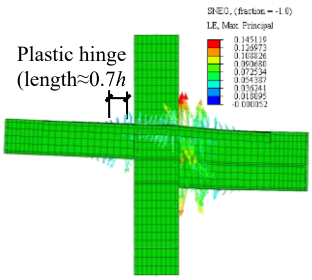

(d) J6-1 (Beam bending-shear failure)

Fig. 11 Typical principal tensile strain distribution

displayed the failure mode D (panel zone shear failure mode), which occurred with a beam end displacement of 50 mm. The first crack was found at the top of the slab when the displacement reached 1.87 mm, which was marked as point A in Fig. 10(a). The longitudinal rebars in the column firstly yielded near the panel zone when $0.5P_y$ was reached, which was marked as point B. Meanwhile, the longitudinal stress of slab rebars was 310 MPa, indicating that the slab rebars were nearly yielded. While the longitudinal stress of beam rebars were still below 300 MPa as well as the Von Mises stress of steel tube, which was far from yielding. The maximum strength was attained at point C as shown in Fig. 10(a) with the displacement reaching $2\Delta_y$. The load in the negative direction was a bit higher than that in the positive direction. It was due to the high stiffness provided by the slab rebars in tension, which has been mentioned in the comparison paper (Ma *et al*. 2019). In Fig. 11(a), The principal strain was focused on the panel zone, which indicated the severe diagonal cracks in the panel zone. The shear strength of the outer concrete decreased to 2.34 MPa and the shear strength of core concrete decreased to 3.68 MPa. Most of the steel components yielded in this loading degree, including the steel tube and stirrups in the panel zone. The bearing capacity decreased to 85% of its maximum value at point D. The panel zone shear strength had a sharp descending branch, which might be due to the concrete spalling and crushing under shear force.

Joint J2-1 behaved the failure mode C (column compression-bending failure mode). The first crack was found at the beam bottom with the displacement reaching 1.14 mm, and it was marked as point A in Fig. 10(b). The longitudinal rebars and the steel tube yielded simultaneously in the column adjacent to the panel zone region when $0.5P_y$ was reached, which was marked as point B in Fig. 10(b). The uniaxial stress of rebars and the Von Mises stress of steel tube in the panel zone were below 280 MPa, indicating that the beam and panel zone remained intact at this loading degree. The maximum strength was attained with the displacement of $2\Delta_y$ at point C. Fig. 11(b) illustrated the principal strain was focused on the column adjacent to the

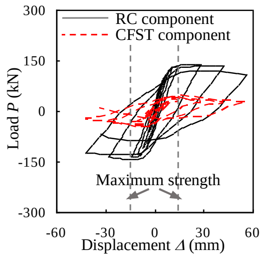

(a) J1-1 (Panel zone shear failure)

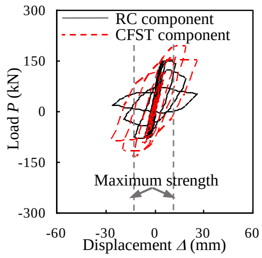

(b) J2-1 (Column compression-bending failure)

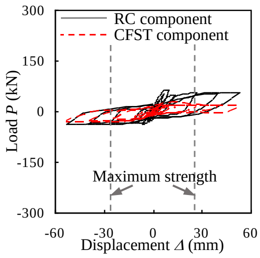

(c) J5-1 (Beam bending failure)

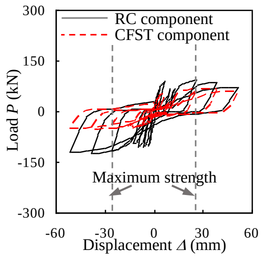

(d) J6-1 (Beam bending-shear failure)

Fig. 12 Typical hysteretic relationships of CFST component and RC component

panel zone, which indicated the severe flexural cracks around that region. The plastic hinge length was approximately equal to 0.5 times of the column sectional height, which was consistent with the test results of joint J2-1. The longitudinal rebars in the beam and steel tube did not yield in this loading degrees, which meant that the beam was much stronger than the column. The load in the negative direction was almost the same as that in the positive direction. Therefore, the maximum strength was controlled by the column section. Point D is the loading degrees that the bearing capacity dropped to 85% of its maximum value. The core concrete compressive strength dropped to 45.12 MPa, while the outer concrete compressive strength dropped to 5.74 MPa. The outer concrete had a sharp drop in the strength, however, the core concrete only had a slight drop in the strength, which could attribute to the high level pressure provided by the steel tube.

Joint J5-1 was the staggered joint with failure mode A (beam bending failure mode), the hysteretic relationship of which was shown in Fig. 10(c). The first crack was found at the beam bottom with the displacement reaching 1.33 mm, which was marked as point A in Fig. 10(c). The beam longitudinal rebars yielded firstly near the panel zone at $0.5P_y$, which was marked as point B in Fig. 10(c). The longitudinal stress of column rebars were below 200 MPa as well as the Von Mises stress of steel tube, indicating that the column and panel zone remain intact at this loading degree. The maximum strength was reached at $3\Delta_y$ in point C in Fig. 10(c). The load was a bit higher in the negative direction than that in the positive direction. It was due to the high stiffness provided by the slab rebars in tension. The principal strain was focused on the beam adjacent to the panel zone as shown in Fig. 11(c), which indicated the severe flexural cracks around the beam end. The plastic hinge length was approximately equal to 0.7 times of the beam sectional height, which was consistent with the test results of joint J5-1. The column longitudinal rebars kept in the elastic stage in this loading degree as well as the steel tube, which meant that the plastic strain accumulated in the beam and developed the plastic hinge. Point D is the loading degree that the bearing capacity decreased to 85% of its maximum value. The highest ever stress of concrete in the column was below 14 MPa, which is less than the uniaxial compressive strength. While the stress of concrete in the beam dropped to 10 MPa at this loading degree. The beam concrete had a sharp drop in the strength, while the concrete in other region did not reach the uniaxial compressive strength.

Joint J6-1 was the unsymmetrical joint, and it displayed the failure mode A and B in the small beam and large beam respectively. Fig. 10(d) showed the typical hysteretic relationships of the large beam in unsymmetrical joints. The first crack was found at the top of the slab when the displacement reached 1.61 mm, which was marked as point A in Fig. 10(d). The longitudinal rebars yielded in both beams adjacent to the panel zone at $0.5P_y$, which was marked as point B in Fig. 10(d). The web rebars of the large beam also yielded in this loading degree. The longitudinal stress of column rebars was below 200 MPa as well as the Von Mises stress of steel tube, indicating that the column and panel zone remained intact at this loading degree. The large beam reached its maximum strength at $2\Delta_y$, while the maximum strength of the small beam was reached at $3\Delta_y$ as shown in Fig. 10(d). The small beam has a lower stiffness than the large beam, therefore the ultimate displacement of the small beam was larger than that of the large beam. The load in the negative direction was a bit higher than that in the positive direction. It was due to the high stiffness provided by the slab rebars in tension. The principal strain

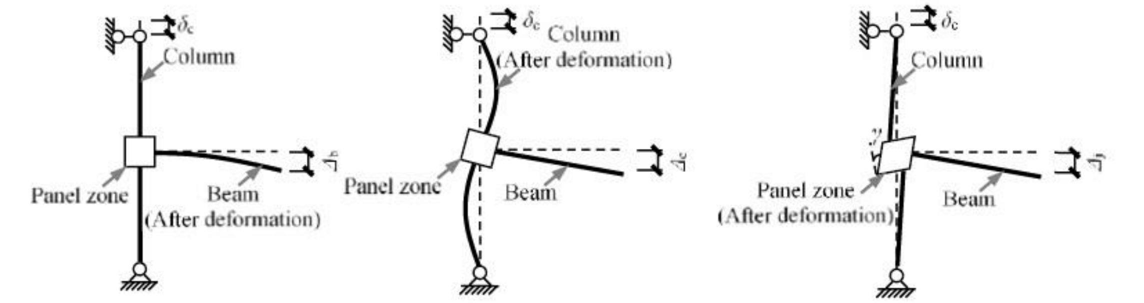

(a) Beam deformation (b) Column deformation (c) Panel zone deformation

Fig. 13 Deformation classification of joint specimens

*Δ_b, Δ_c, Δ_j and represent the beam end deflection caused by the beam deformation, column deformation and panel zone deformation respectively. δ_c and γ represent the column axial compressive deformation and panel zone shear deformation

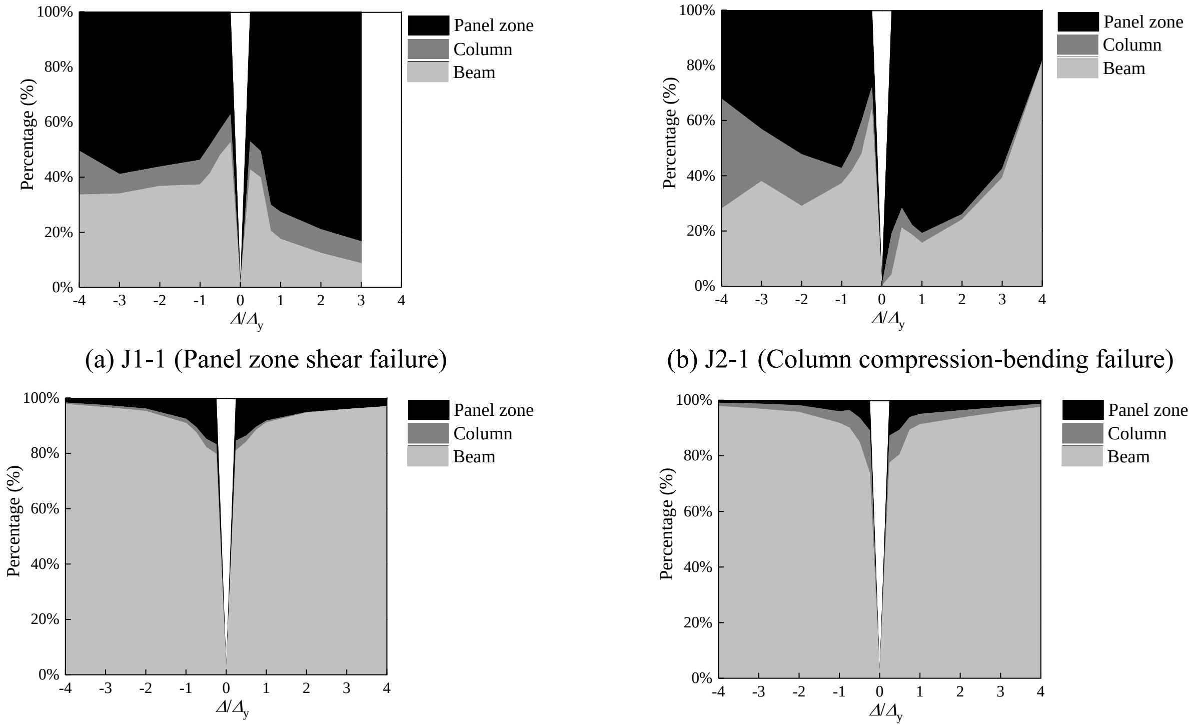

(a) J1-1 (Panel zone shear failure) (b) J2-1 (Column compression-bending failure)

(c) J5-1 (Beam bending failure) (d) J6-1 (Beam bending-shear failure)

Fig. 14 Deformation distributions of joint specimens

was focused on the beam adjacent to the panel zone as shown in Fig. 11(d), which indicated the severe flexural cracks around the small beam and the diagonal cracks around the big beam. The plastic hinge length was approximately equal to 0.7 times small beam sectional height, which was consistent with the test results of joint J6-1. The stirrups in the large beam yielded at this loading degree, which meant that the large beam performed the bending-shear failure mode. Point D is the loading degree that the strength decreased to 85% of its maximum value. The stress of concrete in the large beam dropped to 3.5 MPa and that in the small beam dropped to 21.16 MPa at this loading degree. It indicated that the concrete sustained more degradation from shear failure.

4.2 Hysteretic relationships of components

The bearing capacity and loading stiffness of this composite joint were also highly affected by the combination of the CFST component and RC component in the column (Ma *et al*. 2019). Therefore, the load-displacement relationships of CFST component and RC component were analyzed independently. The column section adjacent to the panel zone was chosen as the typical section and the hysteretic relationships were shown in Fig. 12. The secant stiffness at the yield point was used to justify the loading stiffness.

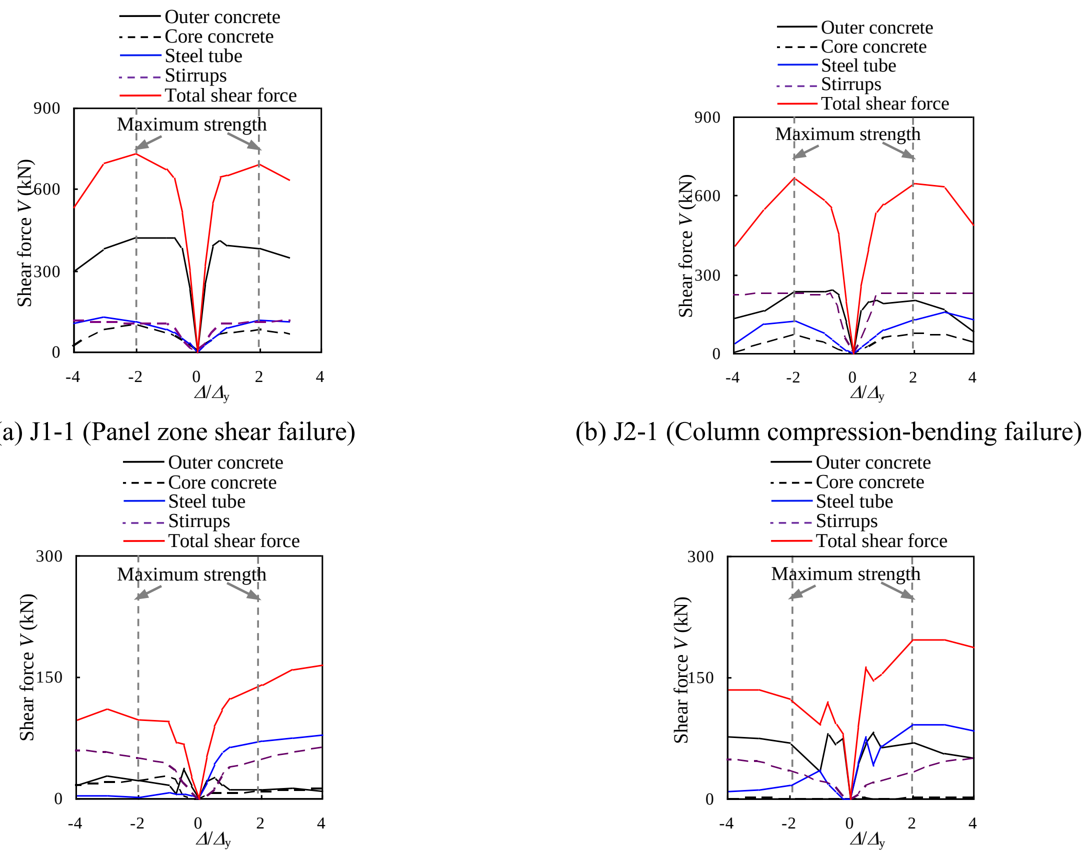

(a) J1-1 (Panel zone shear failure)

(b) J2-1 (Column compression-bending failure)

(c) J5-1 (Beam bending failure)

(d) J6-1 (Beam bending-shear failure)

Fig. 15 Internal shear force distributions in the panel zone

Four typical joints could be classified into two groups. The first group is J2-1 performing failure mode C. Another group is composed of J1-1, J5-1, J6-1. For the first group, the CFST component undertook 163.1kN cyclic load, which was 40.3% higher than the RC component. While the secant stiffness of CFST component was 9.2% lower than the RC component. For the other failure joints, the CFST component undertook much lower cyclic load than the RC component. Taking beam bending failure joint J5-1 as an example, the CFST component undertook 23.5kN cyclic load, which was 54.2% lower than the RC component. Besides, the secant stiffness of CFST component was 52.7% lower than the RC component. To summarize, the CFST component took a more important role in the column failure joints. It could be explained that the CFST component worked together with the RC component. The CFST component located in the centre of the column section and the RC component surrounded the CFST component. The RC component underwent higher stress and strain than the CFST component under the axial load and initial cyclic load. Then, the outer concrete in the RC component firstly reached the maximum stress especially in compression, which let the neutral axis move to the CFST section. Afterwards, the RC component failed to sustain further load and even lost its bearing capacity gradually. Therefore, the CFST component undertook more cyclic load than the RC component in the column failure mode. While the column did not reach the maximum strength in other failure modes, the CFST component could not achieve its potential.

4.3 Deformation distribution

The deformation of joint specimens could be classified into three types of deformation, consisting of beam deformation, column deformation, and panel zone deformation. The schematic view of each type of deformation was shown in Fig. 13. The beam end displacement, contributed by the beam, column and panel zone, were calculated separately based on the FEA model. The deformation distributions of each component were represented by the area in Fig. 14. The bottom region represented the beam deformation. Furthermore, the middle region and the top region represented the column deformation and panel zone deformation separately.

The joint J1-1 behaved failure mode D. The beam underwent large deformation until the yield displacement was reached. The panel zone deformation occupied over 50% of the deformation after the yield displacement. For joint J2-1, the joint showed the failure mode C, while the column deformation was below 10% until the maximum strength was reached. The panel zone and beam held the most deformation. It had two reasons. Firstly, the column had high loading stiffness under high axial load level, which led to a small deformation in the column. Secondly, the CFST component located in the centre of column section

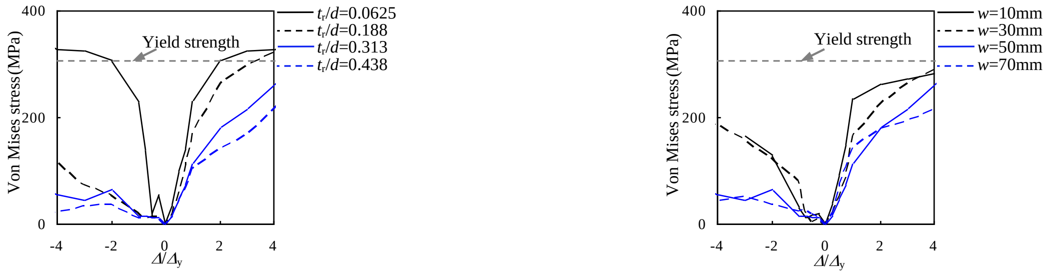

(a) Thickness of ring plate to diameter of longitudinal rebars ratio t_r/d

(b) Width of ring plate w

Fig. 16 Stress development of the ring plate

and acted as a skeleton in the centre. The CFST component could provide extra loading stiffness. Joint J5-1 and joint J6-1 both revealed serious degradation in beam concrete. The plastic hinge was found in the beam adjacent to the panel zone, which led to the failure mode A or failure mode B. It could be found that the beam deformation occupied the most deformation of the joints.

4.4 Interal force distribution

The panel zone was the essential region for beam-column joint. Therefore, the shear strength distribution in the panel zone was analyzed. The panel zone was composed of five parts: core concrete, steel tube, connections, stirrups, longitudinal rebars, and outer concrete. The longitudinal rebars rarely contributed to the shear strength. Therefore, only the shear force sustained by other components were illustrated in Fig. 15.

In general, the failure mode C and D exhibited higher shear strength than failure mode A and B. For joint J1-1, the outer concrete sustained most of the panel zone shear force, and the outer concrete reached its maximum strength at the yield displacement. Afterwards, the shear force carried by outer concrete decreased a bit, while the total shear strength kept increasing from the yield displacement Δ_y to $2\Delta_y$. In this period, the diagonal cracks developed in the outer concrete, and the shear force sustained by the outer concrete decreased. While the shear force sustained by steel components could still increase. After $2\Delta_y$ was reached, the shear force sustained by the outer concrete both decreased together with the core concrete, which led to the failure mode D. The shear force carried by the outer concrete in joint J1-1 was quite larger than that in joint J2-1. In addition, the joint dimension of J2-1 was larger than the joint J1-1. It indicated that the outer concrete in joint J2-1 did not reach its maximum strength. For joint J2-1, the stirrups sustained over 40% of the total shear force, and the remaining shear force was mainly sustained by the steel tube. These two steel components were enough to protect the panel zone from shear failure. Therefore, the outer concrete still had potential resistance and kept intact. For the joint J5-1 and joint J6-1, the shear strength carried by concrete was below 100kN, which was much lower than the joint J1-1. Considering the joint dimension of these two joints were similar to the joint J1-1, the concrete components in the panel zone did not reach the maximum shear strength. The steel components in these two joints could supply enough shear force.

4.5 Constructional details of connections

The beam-column joint studied in this paper is a relatively new type of joint, and the steel tube extends continuously along the column. Since the steel tube runs across the column section, the inner CFST component usually prevents beam longitudinal rebars from going continuously through the panel zone. Therefore, beam longitudinal rebars were fastened to the steel tube by effective connections. The possible connection methods include ring plate connection, sleeve connection, wing plate connection and anchorage connection. The wing plate connection and anchorage connection have been studied by the previous researchers. The sleeve connection has been widely applied in RC structures to connect longitudinal rebars. The dimension and property of sleeve connection have also been required by the corresponding standards (Eurocode 2 1992). Therefore, these three kinds of connections were not analyzed in this paper.

The ring plate connection has rarely been used and studied in the composite joints studied in this paper. The influence of dimension and material property of the ring plate connection needed to be analyzed. Three parameters were selected to present the ring plate connection, including the thickness of ring plate to diameter of longitudinal rebars ratio t_r/d, the width of ring plate w, the yield strength of ring plate f_{yr}. It was found that the yield strength had little effect on the stress development of ring plate, as long as the yield strength of the ring plate was higher than that of the longitudinal rebars and steel tube. Therefore, the yield strength of the ring plate is suggested to be higher than that of longitudinal rebars and steel tube. The stress development of ring plate considering the other two parameters is shown in Fig. 16.

The Von Mises stress of ring plate was found to be usually higher under the positive displacement and lower under the negative displacement, which indicated that the tensile force transferred to the ring plate was higher than the compressive force transferred to the ring plate. The reason is that the concrete contributed more to the compressive force than the tensile force. Fig. 16(a) shows the effects of

Table 2 Parameter ranges of failure modes

Parameters	$0.5 \leq i_b/i_c < 1.5\text{-}2.3$	$1.5\text{-}2.3 \leq i_b/i_c < 3.8\text{-}4.5$	$i_b/i_c \geq 3.8\text{-}4.5$
$2\text{-}3 \leq \lambda_b \leq 5$	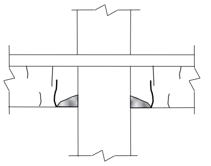 Beam bending failure	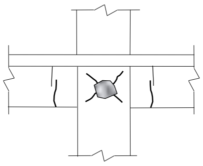 Panel zone shear failure	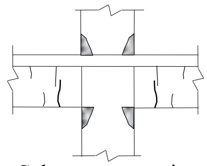 Column compression-bending failure
$1.5\text{-}1.8 \leq \lambda_b < 2\text{-}3$	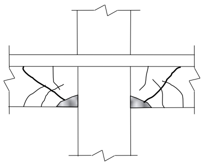 Beam bending-shear failure	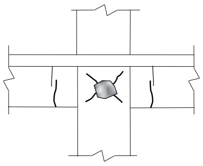 Panel zone shear failure	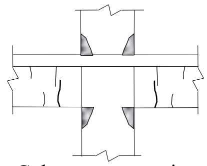 Column compression-bending failure
$0.5 \leq \lambda_b < 1.5\text{-}1.8$	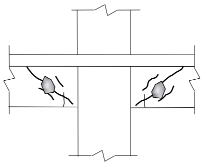 Beam shear failure	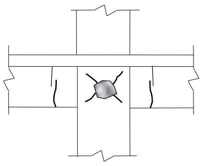 Panel zone shear failure	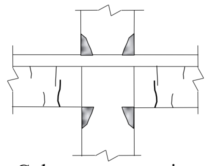 Column compression-bending failure

the thickness of ring plate to diameter of longitudinal rebars ratio t_r/d. The stress of the ring plate increased as t_r/d decreased, which was due to the sectional area reduction of the ring plate. It could be found that the ring plate yielded when the t_r/d was under 0.313. The connections were supposed to be intact before the joint failed in the design of the beam-column joint. Therefore, it was suggested that t_r/d should be higher than 0.35. Meanwhile, the diameter of the beam longitudinal rebars was usually less than 50 mm in construction. Considering the matching of ring plate, the t_r/d should be between 0.35 and 1.00. The effects of the width of the ring plate w are shown in Fig. 16(b). The stress of the ring plate was approximated to the yield strength with the width lower than 30 mm, which is about 2.14d. Besides, the ring plate needed to provide enough welding length for beam longitudinal rebars. Therefore, the width of the ring plate was suggested to be higher than 2.5d. Considering the layout of reinforcements in the panel zone and the constructional space, the sectional width of column B is suggested to be larger than 700 mm. Meanwhile, the constructional space between the ring plate and column stirrups should be larger than 50 mm. Therefore, it is suggested that the width of the ring plate should be higher than 2.5d mm and lower than $(B\text{-}D)/2\text{-}50$ mm.

4.6 Failure modes prediction

According to the analysis mentioned above, the strength, ductility and energy dissipation varied much among different failure modes. Accordingly, this paper aimed to propose a failure modes prediction method for the beam-column joint. Although the bearing capacity of different components could classify different failure modes theoretically, the calculation for the bearing capacity of various components was quite complicated, especially for the concrete-encased CFST column and its panel zone. The column had a composite section and needed to account for the contribution of each component. Moreover, the confinement effects from both the steel tube and stirrups profoundly affected the bearing capacity, which needed to be further studied. The existing calculation method was compared with the test results, as shown in Table 1. It was found that the calculated beam and column strength agreed well with the test results. However, the two types of the calculation method for the panel zone shear strength were inconsistent with each other, and both of them were not accurate enough to predict the failure mode for specimen J4-1, J4-2 and J4-3. Consequently, a simplified method was needed to predict failure modes. Based on the failure mode prediction method, the brittle failure could be prevented, and the failure region could be conveniently controlled in the structural design.

A typical panel zone shear failure joint with square column section was established based on the verified model. Then the parameter studies were conducted to figure out the failure mode prediction method. The parameter ranges included: Cube strength of core concrete $f_{cu,core}$ = 40-80 MPa; Cube strength of outer concrete $f_{cu,out}$ = 40-60 MPa; Steel tube ratio α_s =0.05-0.20; Confinement factor ξ=1-3; Yield strength of column stirrup f_{yhc} = 300-400 MPa; Yield strength of column longitudinal rebar f_{ylc} = 300-400 MPa; Column volumetric stirrup ratio ρ_{vc} = 0.50%-2.00%; Column longitudinal rebar ratio ρ_{sc} = 1.00%-2.00%; Diameter of steel tube to sectional width ratio D/B = 0.40-

0.75; Axial load level n = 0.1-0.6; Yield strength of beam stirrup f_{yhb} = 300-400 MPa; Yield strength of beam longitudinal rebar f_{ylb} = 300-400 MPa; Beam volumetric stirrup ratio ρ_{vb} = 1.00%-2.00%; Beam longitudinal rebar ratio ρ_{sb} = 1.00%-2.00%; Beam shear span ratio λ_b = 0.5-5; Beam to column linear bending stiffness ratio i_b/i_c = 0.5-4.5. The beam to column linear bending stiffness ratio i_b/i_c could be calculated by Eqs.1-3, in which the stiffness contribution of steel tube was considered.

$$i_b = (EI)_b/l_b \tag{1}$$

$$i_c = (EI)_c/l_c \tag{2}$$

$$(EI)_c = E_c I_c + E_s I_s \tag{3}$$

After a large number of calculated examples, it was found that the beam to column linear bending stiffness ratio i_b/i_c could somehow represent the beam to column strength ratio. It basically has three reasons: (i) the modulus of elasticity E and the second moment of area I have a positive correlation with the material strength and the effective section modulus respectively. Moreover, the material strength and the effective section modulus could indicate the bending strength of the beam and column to a certain degree. Since the failure modes largely depend on the beam to column strength ratio, the linear bending stiffness ratio i_b/i_c needed to be considered in predicting the failure mode; (ii) the linear bending stiffness usually determines the internal force of beam or column specimens in the frame structures; (iii) the ductility often governed the design of structures in seismic zones (Emam *et al*. 1997), which was also highly influenced by the stiffness. The concrete-encased CFST column had an advantage in reducing sectional dimension compared to the conventional RC column with same bearing capacity. While the smaller section would consequently lead to a smaller stiffness (Qian *et al*. 2016). The stiffness needs to be taken into account in designing this kind of composite joint. Therefore, the linear bending stiffness ratio i_b/i_c was applied to classify the failure region, i.e., beam, column and panel zone. Furthermore, the shear span ratio λ_b was found to be the most critical parameter that affected the beam failure mode within the limited study. It could be used to distinguish between the failure mode A and B according to the parametric studies. A large amount of parameter analysis was conducted to determine the parameter ranges of failure modes. It was found that these two parameters could predict the failure modes to a large extent. Although other aforementioned parameters also had appropriate effects on the failure modes, the effects caused by these parameters could be considered in the range of the beam to column linear bending stiffness ratio i_b/i_c and shear span ratio λ_b. Therefore, the failure modes could be predicted by considering the range of these two parameters within the studied parameter range, which was shown in Table 2.

5. Conclusions

Within the scope of the limited parametric studies, the following conclusions could be drawn in this paper:

- The seismic performance of the concrete-encased CFST column to RC beam joint was investigated analytically, which could consider the deterioration of concrete, Baushinger effects of steel components, slippage of longitudinal rebars as well as the discrete cracking. Taking the aforementioned factors into consideration, the proposed model could reveal the seismic performance of the beam-column joints.
- Four kinds of joint failure modes were investigated under the full-range analysis. Four characteristic points were selected to represent the critical moment during the loading procedure and the corresponding stress status of steel and concrete components were analyzed. The deformation and internal force distribution of the panel zone were analyzed under four failure modes. For the panel zone shear failure, the panel zone deformation occupied over 50% of the deformation after the yield displacement, and the shear force was mostly undertaken by the outer reinforced concrete, which is quite larger than that in other failure modes.
- The sleeve connection, wing plate connection, as well as anchorage connection, could refer to the corresponding standards. The influence of dimension and material property of the ring plate connection was analyzed through the FEA model. It is suggested that (i) the yield strength of the ring plate be higher than that of beam longitudinal rebars, (ii) the thickness of the ring plate to diameter of longitudinal rebars ratio t_r/d be between 0.35 and 1.00, (iii) the width of ring plate w be higher than 2.5d mm but be lower than (B-D)/2-50 mm.
- A large number of calculated examples were established to determine the key parameters affecting the failure modes. The linear bending stiffness ratio i_b/i_c and shear span ratio λ_b were identified as key parameters among 16 parameters. The failure modes could be predicted in this paper within the limited parameters. The shear strength model of panel zone needs to consider the strength contribution of each component and the confinement effects, which could be proposed in further study.

Acknowledgments

The research reported in this paper is part of the Project 51678341 supported by the National Natural Science Foundation of China (NSFC). The financial support is highly appreciated.

References

ACI 318 (2014), Building code requirements for structural concrete and commentary, American Concrete Institute; Farmington Hills, MI, USA.

An, Y.F. and Han L.H. (2014), "Behaviour of concrete-encased CFST columns under combined compression and bending", *J.*

Constr. Steel. Res., **101**, 314-330. https://doi.org/10.1016/j.jcsr.2014.06.002.

Attard, M.M. and Setunge, S. (1996), "Stress-strain relationship of confined and unconfined concrete", *ACI Mater. J.*, **93**(5), 432-442.

CECS 188 (2019), Technical specification for steel tube-reinfo rced concrete column structures, China Association for Eng ineering Construction Standardization; Beijing, China. (in C hinese).

Chen, Q.J., Cai, J., Bradford, M.A., Liu, X. and Zuo, Z.L. (2014), "Seismic behaviour of a through-beam connection between concrete-filled steel tubular columns and reinforced concrete beams", *Eng. Struct.*, **80**, 24-39. https://doi.org/10.1016/j.engstruct.2014.08.036.

Clough R.W. (1966), "Effect of Stiffness Degradation on Earthquake Ductility Requirements", Structural Engineering Laboratory, University of California, Berkeley, CA, USA.

De Nardin, S. and El Debs, A.L.H. (2018), "Shear transfer mechanism in connections involving concrete filled steel columns under shear forces", *Steel Compos. Struct.*, **28**(4), 449-460. https://doi.org/10.12989/scs.2018.28.4.449.

De Risi, M.T. and Verderame, G.M. (2017), "Experimental assessment and numerical modelling of exterior non-conforming beam-column joints with plain bars", *Eng. Struct.*, **150**, 115-134. https://doi.org/10.12989/eas.2017.12.1.119.

Emam, M., Marzouk, H. and Hilal, M.S. (1997), "Seismic response of slab-column connections constructed with high-strength concrete", *ACI Struct. J.*, **94**, 197-205.

Eurocode (2004), Design of concrete structures-Part 1-1: General rules and rules for buildings, European Committee for Standardization; Brussels, Belgium.

Goto, Y., Kumar, G.P. and Kawanishi, N. (2010), "Nonlinear finite-element analysis for hysteretic behavior of thin-walled circular steel columns with in-filled concrete", *J. Struct. Eng.-ASCE*, **136**(11), 1413-1422. https://doi.org/10.1061/(ASCE)ST.1943-541X.0000240.

Han, L.H. and Yang, Y.F. (2005), "Cyclic performance of concrete-filled steel CHS columns under flexural loading", *J. Constr. Steel. Res.*, **61**(4), 423-452. https://doi.org/10.1016/j.jcsr.2004.10.004.

Han, L.H., Yao, G.H. and Tao, Z. (2007), "Performance of concrete-filled thin-walled steel tubes under pure torsion", *Thin Wall Struct.*, **45**(1), 24-36. https://doi.org/10.1016/j.tws.2007.01.008.

Han, L.H. and An, Y.F. (2014), "Performance of concrete-encased CFST stub columns under axial compression", *J. Constr. Steel. Res.*, **93**, 62-76. https://doi.org/10.1016/j.jcsr.2013.10.019.

Han, L.H., Ma, D.Y. and Zhou, K. (2018), "Concrete-encased CFST structures: behaviour and application", Proceeding of the 12th International Conference on Advances in Steel-Concrete Composite Structures (ASCCS 2018), València, Spain, June.

Hwang, H.J., Eom, T.S. and Park, H.G. (2017), "Shear Strength Degradation Model for Performance-Based Design of Interior Beam-Column Joints", *ACI Struct. J.*, **114**(5), 1143-1154. https://doi.org/10.14359/51700780.

Kang, L., Leon, R.T. and Lu, X. (2015), "Shear strength analyses of internal diaphragm connections to CFT columns", *Steel Compos. Struct.*, **18**(5), 1083-1101. https://doi.org/10.12989/scs.2015.18.5.1083.

Kang, S.B. and Tan, K.H. (2018), "A simplified model for reinforced concrete beam-column joints under seismic loads", *Mag. Concrete Res.*, **70**(3) 138-153. https://doi.org/10.1680/jmacr.16.00074.

Lai, Z., Huang, Z. and Varma, A.H. (2017), "Modeling of high-strength composite special moment frames (C-SMFs) for seismic analysis", *J. Constr. Steel Res.*, **138**, 526-537. https://doi.org/10.1016/j.jcsr.2017.07.018.

Lee, J.Y., Kim, J.Y. and Oh, G.J. (2009), "Strength deterioration of reinforced concrete beam–column joints subjected to cyclic loading", *Eng. Struct.*, **31**(9), 2070-2085. https://doi.org/10.1016/j.engstruct.2009.03.009.

Li, B. and Leong, C.L. (2014), "Experimental and numerical investigations of the seismic behavior of high-strength concrete beam-column joints with column axial load", *J. Struct. Eng. - ASCE*, **141**(9), 04014220. https://doi.org/10.1061/(ASCE)ST.1943-541X.0001191.

Li, W. and Han, L.H. (2011), "Seismic performance of CFST column to steel beam joints with RC slab: Analysis", *J. Constr. Steel Res.*, **67**(1), 127-139. https://doi.org/10.1016/j.jcsr.2010.07.002.

Lima, C., Martinelli, E., Macorini, L. and Izzuddin, B.A. (2017), "Modelling beam-to-column joints in seismic analysis of RC frames", *Earthq. Struct.*. **12**(1), 119-133. https://doi.org/10.12989/eas.2017.12.1.119.

Lee, J. and Fenves, G.L. (1998), "Plastic-damage model for cyclic loading of concrete structures", *J. Eng. Mech. - ASCE*, **124**(8), 892-900. https://doi.org/10.1061/(ASCE)0733-9399(1998)124:8(892).

Ma, D.Y., Han, L.H., Li, W. and Zhao, X.L. (2017), "Seismic performance of concrete-encased CFST piers: analysis", *J. Bridge Eng.-ASCE*, **23**(1), 04017119. https://doi.org/10.1061/(ASCE)BE.1943-5592.0001157.

Ma, D.Y., Han, L.H., Ji, X. and Yang, W.B. (2018), "Behaviour of hexagonal concrete-encased CFST columns subjected to cyclic bending", *J. Constr. Steel Res.*, **144**, 283-294. https://doi.org/10.1016/j.jcsr.2018.01.019.

Ma, D.Y., Han, L.H. and Zhao, X.L. (2019), "Seismic performance of the concrete-encased CFST column to RC beam joint: Experiment", *J. Constr. Steel Res.*, **154**, 134-148. https://doi.org/10.1016/j.jcsr.2018.11.030.

Moustafa, M.A. and Mosalam, K.M. (2015), "Seismic response of bent caps in as-built and retrofitted reinforced concrete box-girder bridges", *Eng. Struct.*, **98**, 59-73. https://doi.org/10.1016/j.engstruct.2015.04.028.

Qian, W.W. (2017), "Seismic Performance of Concrete-encased Concrete-filled Steel Tubular Column to Steel Beam Joints", PhD. Dissertation; Tsinghua University, Beijing, China.

Qian, W.W., Li, W., Han, L.H. and Zhao, X. L. (2016), "Analytical behavior of concrete-encased CFST columns under cyclic lateral loading", *J. Constr. Steel Res.*, **120**, 206-220. https://doi.org/10.1016/j.jcsr.2015.12.018.

Shen, J.M., Wang, C.Z. and Jiang, J.J. (1993), Finite Element Method of Reinforced Concrete and Limited Analysis of Plates and Shells, Tsinghua University Press, Beijing, China. (in Chinese).

Simulia (2017), ABAQUS Version 2017-1: theory manual, users' manual, verification manual and example problems manual.

Zhang, Y., Huang, Y., Lei, K., Pei, J. and Zhang, Q. (2018), "Seismic behaviors of steel bar reinforced joints of concrete filled steel tubular laminated columns", *KSCE J. Civil Eng.*, **22**(9), 3491-3503. https://doi.org/10.1007/s12205-017-0685-8.

CC

Nomenclature

A_{core}	Cross-sectional area of core concrete
A_s	Cross-sectional area of steel tube
B	Width of column
D	Diameter of steel tube
d	Diameter of longitudinal rebars
d_c	Compressive damage variable
d_t	Tensile damage variable
EI_b	Beam bending stiffness
EI_c	Column bending stiffness
E_c	Modulus of elasticity of concrete
E_s	Modulus of elasticity of steel
f_c'	Cylinder strength of concrete
$f_{c,core}$	Prismatic strength of core concrete
$f_{cu,core}$	Cube strength of core concrete
$f_{cu,out}$	Cube strength of outer concrete
f_{yhb}	Yield strength of beam stirrup
f_{yhc}	Yield strength of column stirrup
f_{ylb}	Yield strength of beam longitudinal rebar
f_{yhc}	Yield strength of column longitudinal rebar
f_{yr}	Yield strength of ring plate
f_{ys}	Yield strength of steel tube
i_b	Beam linear bending stiffness ($= EI_b/l_b$)
i_c	Column linear bending stiffness ($= EI_c/l_c$)
I_c	Moment of inertia of concrete section;
I_s	Moment of inertia of steel tube section;
l_b	Distance between rotating centers of beam
l_c	Distance between rotating centers of column
n	Axial load level($=N_0/N_u$)
N_0	Constant axial load
N_u	Axial Compressive strength
P	Vertical cyclic load
P_y	Yield strength of joints
P_{uc}	Predicted maximum strength of joints
P_{ue}	Measured maximum strength of joints
t	Steel tube thickness of CFST
t_r	Thickness of ring plate
V	Shear force
w	Width of ring plate
α_s	Steel ratio of CFST section ($= A_s/A_{core}$)
Δ	Vertical cyclic displacement
Δ_y	Yield displacement
ξ	Confinement factor for CFST section ($= \alpha_s f_{ys}/f_{c,core}$)
λ_b	Beam shear span ratio
μ	Frictional factor
ρ_{sc}	Column longitudinal rebar ratio
ρ_{sb}	Beam longitudinal rebar ratio
ρ_{vc}	Column volumetric stirrup ratio
ρ_{vb}	Beam volumetric stirrup ratio
σ_{c0}	Uniaxial compressive strength of concrete
σ_{t0}	Uniaxial tensile strength of concrete
ω_c	Compressive stiffness recovery factor
ω_t	Tensile stiffness recovery factor